

## Planar graphene-NbSe<sub>2</sub> Josephson junctions in a parallel magnetic field

Tom Dvir<sup>1,\*</sup>, Ayelet Zalic<sup>1,\*</sup>, Eirik Holm Fyhn<sup>2</sup>, Morten Amundsen<sup>2</sup>, Takashi Taniguchi<sup>3</sup>, Kenji Watanabe<sup>4</sup>,  
Jacob Linder<sup>2</sup> and Hadar Steinberg<sup>1</sup>

<sup>1</sup>*The Racah Institute of Physics, The Hebrew University of Jerusalem, Jerusalem 91904, Israel*

<sup>2</sup>*Center for Quantum Spintronics, Department of Physics, Norwegian University of Science and Technology, NO-7491 Trondheim, Norway*

<sup>3</sup>*International Center for Materials Nanoarchitectonics, National Institute for Materials Science, 1-1 Namiki, Tsukuba 305-0044, Japan*

<sup>4</sup>*Research Center for Functional Materials, National Institute for Materials Science, 1-1 Namiki, Tsukuba 305-0044, Japan*



(Received 9 August 2020; revised 26 January 2021; accepted 28 January 2021; published 2 March 2021)

Thin transition metal dichalcogenides sustain superconductivity at large in-plane magnetic fields due to Ising spin-orbit protection, which locks their spins in an out-of-plane orientation. Here we use thin NbSe<sub>2</sub> as superconducting electrodes laterally coupled to graphene, making a planar, all van der Waals two-dimensional Josephson junction (2DJJ). We map out the behavior of these novel devices with respect to temperature, gate voltage, and both out-of-plane and in-plane magnetic fields. Notably, the 2DJJs sustain supercurrent up to parallel fields as high as 8.5 T, where the Zeeman energy  $E_Z$  rivals the Thouless energy  $E_{Th}$ , a regime hitherto inaccessible in graphene. As the parallel magnetic field  $H_{\parallel}$  increases, the 2DJJ's critical current is suppressed and in a few cases undergoes suppression and recovery. We explore the behavior in  $H_{\parallel}$  by considering theoretically two effects: a  $0-\pi$  transition induced by tuning of the Zeeman energy and the unique effect of ripples in an atomically thin layer which create a small spatially varying perpendicular component of the field. The 2DJJs have potential utility as flexible probes for two-dimensional superconductivity in a variety of materials and introduce high  $H_{\parallel}$  as a newly accessible experimental knob.

DOI: [10.1103/PhysRevB.103.115401](https://doi.org/10.1103/PhysRevB.103.115401)

### I. INTRODUCTION

By coupling graphene to exfoliated superconductors such as NbSe<sub>2</sub> [1–3] it is possible to realize Josephson junctions where both the normal and superconductor materials are two-dimensional (2D). Such junctions should sustain high in-plane magnetic fields. Thin NbSe<sub>2</sub> retains superconductivity at very high in-plane fields due to a combination of suppressed orbital depairing and Ising protection against pair breaking [4,5] and can sustain magnetic fields above 8 T without any measurable effect on the gap size [4,6]. Coupling graphene to two NbSe<sub>2</sub> flakes results in an all van der Waals two-dimensional Josephson junction (2DJJ). The response of such 2DJJs to in-plane magnetic field will be dictated by both spin and orbital effects. In the graphene layer, forming the weak link, the response of carrier spins to the Zeeman field may lead to interesting phenomena such as finite-momentum Cooper pairing and a  $0-\pi$  transition [7–10]. However, the deviation of such devices from the ideal 2D geometry due to ripples and other deformations is significant, as it gives rise to field components perpendicular to the local sample plane, introducing orbital dephasing. The latter also occurs due to the bending of magnetic field flux lines, which cannot be considered truly parallel, as they are deflected by superconducting leads [11].

Two-dimensional Josephson devices are a useful platform for the study of finite-momentum superconducting states: Cooper pairs may survive in the spin-polarized Fermi surface

created at high magnetic fields by attaining a finite center-of-mass momentum [12,13], which translates into a spatially varying order parameter. Finite Cooper-pair momentum  $q = 2E_Z/\hbar v_F$  is dictated by the Zeeman energy  $E_Z = 0.5g\mu_B H$ , where  $g$  is the Landé factor,  $v_F$  is the Fermi velocity, and  $\mu_B$  is the Bohr magneton. The resulting oscillation of the order parameter within the junction can create  $\pi$ -phase junctions, where the transition to the  $\pi$  phase is found in junction lengths  $L$  determined by the multiples of  $\pi/q$ . Weak links characterized by large  $g$  factors have shown signatures of finite-momentum Cooper pairing [14] and allowed the realization of tunable Zeeman-driven  $0-\pi$  transitions [15–17]. Graphene should also exhibit a Zeeman-driven  $0-\pi$  transition [7–10]. However, reaching this transition requires the application of high magnetic fields due to the low  $g$  factor which limits the momentum shift of the Cooper pair. Ballistic graphene is uniquely expected to produce field-tunable switching between  $0$  and  $\pi$  phases while retaining a finite critical current [7] and is expected to exhibit triplet superconductivity [18].

However, the entirely 2D nature of the graphene sheet gives rise to a unique form of disorder due to graphene ripples in the third dimension. In the presence of applied  $H_{\parallel}$  this introduces a small component of perpendicular field with a disorderly spatial variation created by the ripple pattern. This effect can lead to critical current decay with parallel field, a non-Fraunhofer interference pattern, and suppression and recovery of the critical current mimicking a  $0-\pi$  transition. The effect of ripples changes depending on ripple amplitude and wavelength and junction dimensions [19]. Thus, in any

\*These authors contributed equally to this work.

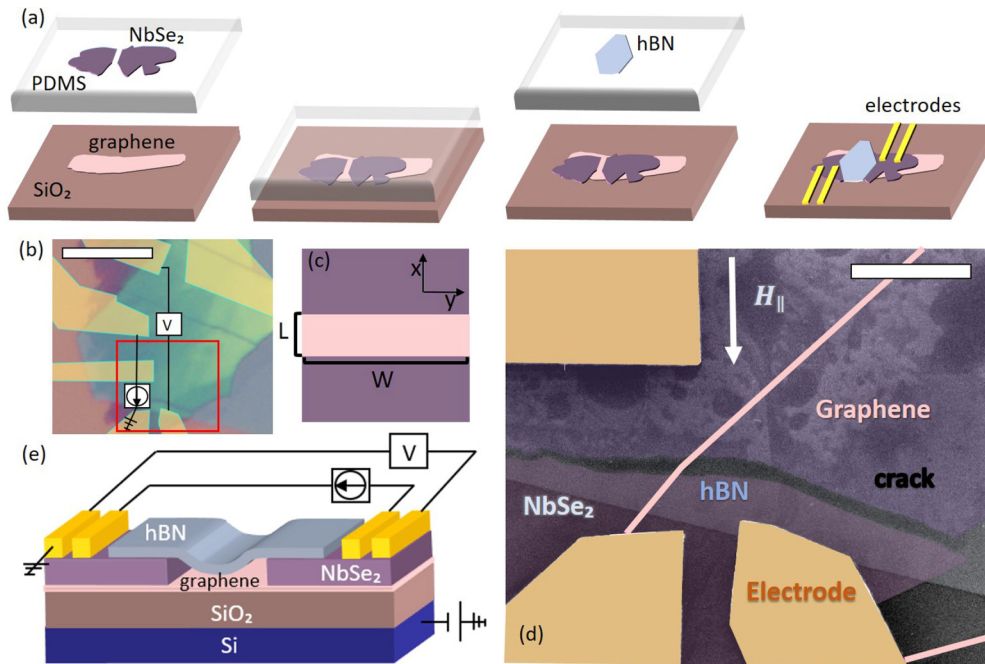


FIG. 1. (a) Fabrication of planar graphene-NbSe<sub>2</sub> JJs involves (1) exfoliation of graphene on SiO<sub>2</sub> and NbSe<sub>2</sub> on PDMS, (2) stamping a cracked NbSe<sub>2</sub> flake onto graphene, (3) stamping a thin hBN flake for encapsulation of the crack, (4) and patterning of electrodes. Steps are illustrated from left to right. (b) Optical image of junction A with schematics of current flow. NbSe<sub>2</sub> thickness is around 10 nm. Scale bar is 10 μm. (c) Illustration of a rectangular junction geometry. (d) A false-color SEM image of the region marked by a red square in (b), showing the actual junction geometry, with the graphene flake contour highlighted and the direction of  $H_{\parallel}$  indicated. Scale bar is 2 μm. (e) Schematic illustration of the JJ in a four-probe electronic configuration. Current flows in plane from NbSe<sub>2</sub> to graphene to NbSe<sub>2</sub>. The crack is shielded from the top by hBN. Gate voltage is applied across the SiO<sub>2</sub> dielectric.

experiment involving graphene in a parallel field—or, indeed, we believe any 2D conductor in a parallel field—this effect should be considered. The morphology and effect of ripples are expected to change depending on the substrate and thickness of the 2D layer. Due to the high parallel fields sustained by the junction, our 2DJJ is sensitive to both long- and short-wavelength submilliradian curvature and subnanometer height variation in graphene.

We study planar NbSe<sub>2</sub>-graphene-NbSe<sub>2</sub> junctions, fabricated by transferring cracked NbSe<sub>2</sub> on exfoliated graphene (see Fig. 1 and detailed information in the Supplemental Material, Sec. 4 [20]). The thickness of the NbSe<sub>2</sub> flakes used for the devices in this paper was around 5–10 nm, evaluated by optical contrast. The junctions exhibit supercurrent characteristics which are similar to diffusive graphene-based devices fabricated using evaporated superconducting electrodes, including gate-tunable critical current and a Fraunhofer-like interference in out-of-plane field [21–25]. Upon application of in-plane field, the 2DJJ critical current undergoes exponential suppression and transitions from a Fraunhofer to superconducting quantum interference device (SQUID)-like interference pattern, which is retained as the field is further increased up to 8.5 T. We focus our paper on junction A, with NbSe<sub>2</sub> thickness of around 10 nm and a weak link consisting of monolayer graphene. In this device we find that the supercurrent exhibits a pronounced suppression-recovery pattern, a feature which may be associated either with a 0- $\pi$  transition or with the effect of graphene ripples.

## II. TRANSPORT MEASUREMENTS

We begin by characterizing the transport of a 2DJJ. Figure 2(a) shows the typical current-voltage characteristics of junction A, where the  $I$ - $V$  curves at different gate voltages exhibit a switching behavior between zero resistance and finite resistance at the junction switching current  $I_C$ . Typical of density-tunable graphene JJs [21],  $I_C$  is modulated by the gate voltage  $V_G$  and reaches a minimal, yet finite, value of  $I_C \approx 0.4 \mu\text{A}$  at the Dirac point  $V_G = -4$  V. This is evident in Fig. 1(b), where the differential resistance  $dV/dI$  vs  $I$  and  $V_G$  is presented as a color plot. Thus, our 2DJJs exhibit the same bipolar supercurrent expected in graphene-based Josephson devices [21].

The Thouless energy  $E_{Th}$ , defined as the inverse of the traversal time of the junction, is an energy scale characteristic of normal transport, which also governs the superconducting properties of Josephson junctions [27]. Josephson junctions vary between regimes defined as long ( $\Delta/E_{Th} \gg 1$ ) or short ( $\Delta/E_{Th} \ll 1$ ) and diffusive ( $L > l$ ) or ballistic ( $L < l$ ), where  $l$  is the mean free path in the weak link and  $L$  is the junction length. In the diffusive case  $E_{Th} = \hbar D/L^2$ , where  $D$  is the diffusion constant and  $L$  is the junction length.  $E_{Th}$  and  $l$  can, in principle, be extracted from the dependence of graphene normal resistance on  $V_G$  [24,25]. However, our device has an unusual geometry and noncolinear current and voltage probes, introducing uncertainties in the determination of  $E_{Th}$ . Taking  $l$  in the tens of nanometers, we estimate  $E_{Th}$  to be a few hundred  $\mu\text{eV}$ . The gap  $\Delta$  of 10-nm-thick NbSe<sub>2</sub> is close to the bulk

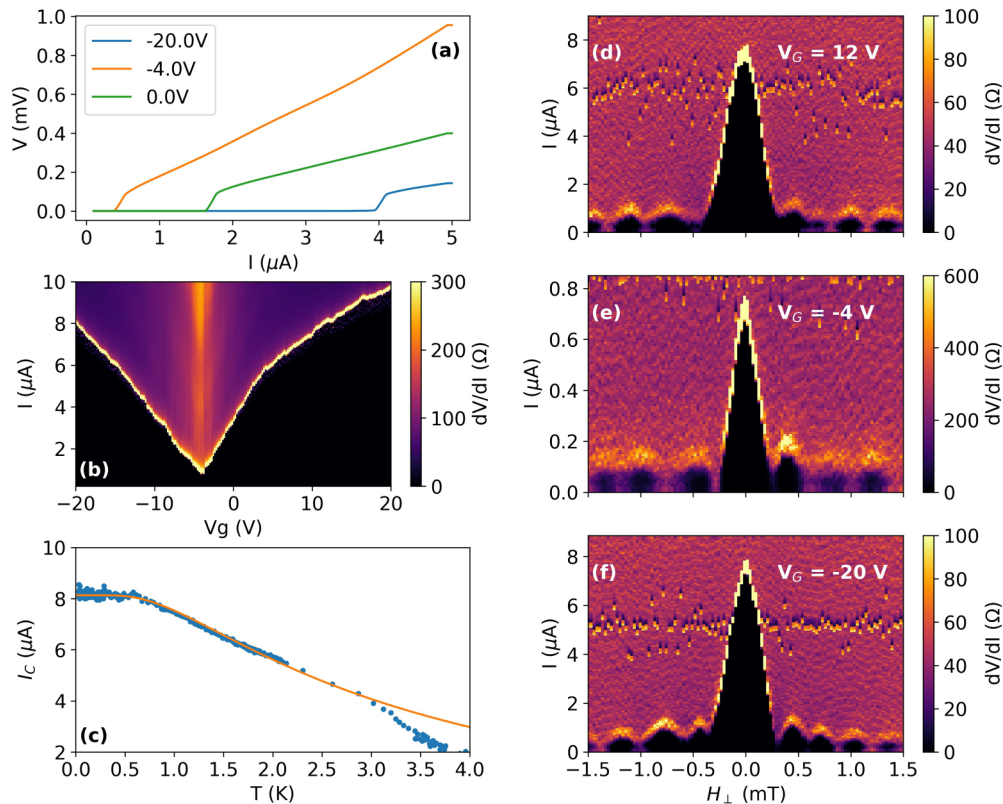


FIG. 2. (a)  $I$ - $V$  curves of junction A (monolayer graphene) taken at different gate voltages (see legend). (b) Differential resistance  $dV/dI$  of junction A as a function of bias current and gate voltage. (c) Temperature dependence of the critical current of junction A (blue dots) and a fit to Eq. (1) (orange line), taken with a gate voltage of  $-20$  V. (d)–(f) Differential resistance of junction A as a function of bias current and external perpendicular magnetic field, taken with gate voltages of 12 V,  $-4$  V (Dirac point), and  $-20$  V, respectively. All the panels show data at  $H_{\parallel} = 0$  T and  $T = 30$  mK.

value of 1.3 meV [28], placing junction A in an intermediate regime, leaning towards the long and diffusive.

It is predicted that in infinitely long metallic diffusive superconductor-normal-superconductor (SNS) junctions, with perfect contacts, at zero temperature  $eI_C R_N = \alpha E_{Th}$  ( $R_N$  is the junction normal resistance [29]). Values near the theoretically predicted value of  $\alpha = 10.82$  were seen in metal SNS junctions [29], whereas in graphene  $\alpha$  varies widely, reaching values as much as 100 times smaller than theory [22–25]. Low values of  $\alpha$  are attributed to an effective Thouless energy  $E_{Th}^*$ , smaller than  $E_{Th}$  determined by transport. This is possibly due to finite contact resistance and Andreev reflections across the N-S barrier, which increase the time of junction traversal [25,26]. In junction A  $E_{Th}$  is of the order of  $I_C R_N$ ; thus, the proportionality factor  $\alpha$  is of order unity. This indicates an effective  $E_{Th}^* \approx 0.1 E_{Th}$ , smaller than metallic SNS junctions and larger than previously reported diffusive graphene junctions [22–25].

In the long junction limit at low temperatures theory predicts [29]

$$eI_C R_N = \alpha_1 E_{Th} \left[ 1 - b \exp\left(\frac{-\alpha_2 E_{Th}}{3.2 k_B T}\right) \right], \quad (1)$$

where  $\alpha_1 = \alpha_2 = 10.82$  and  $b = 1.3$ . Previous attempts to fit the temperature dependence in superconductor-graphene-superconductor (SGS) junctions led to findings of  $\alpha_{1,2} = 1.1$ – $2.9$  in [3,22,25]. In Fig. 2(c) we show that the temperature

dependence of the critical current in junction A fits well to an equation of this form at low temperatures up to  $T \simeq 3$  K. Since we do not know the precise value of the transport  $E_{Th}$ , the fitting parameters are of limited quantitative value; nevertheless, assuming  $E_{Th} \approx 300 \mu\text{eV}$ , we find  $\alpha_1 = 1.2$ ,  $\alpha_2 = 2.4$ , and  $b = 1.2$ . ( $\alpha_1 < \alpha_2$  was also found for similar NbSe<sub>2</sub>-graphene JJs [17]). These values of  $\alpha_{1,2} < 10.82$  again indicate an effective  $E_{Th}^* < E_{Th}$ . As we will show below, measurements at parallel magnetic fields may provide another gauge for  $E_{Th}^*$ .

Next, we observe the response of the system to the application of magnetic field  $H_{\perp}$  perpendicular to the junction plane. Figures 2(d)–2(f) show  $dV/dI$  as a function of  $H_{\perp}$  and  $I$ , taken at three different gate voltages. The observed Fraunhofer-like pattern confirms a smooth current distribution across the junction. The apparent period is 0.4 mT. We compare this to the expected period  $\Phi_0 / [(L + 2\lambda_L)W]$ , where  $\Phi_0$  is the flux quantum,  $L$  is the average junction length, and  $W$  is the junction width.  $\lambda_L$  is the London penetration length, taken to be  $\lambda_L = 200$  nm (known values in the literature range between  $\approx 120$  nm for bulk NbSe<sub>2</sub> [30] and 250 nm for bilayer NbSe<sub>2</sub> [31]). Using the above, we find the period to be  $\approx 0.7$  mT: larger than the observed period, likely due to flux focusing [11,23].

The junction appears to retain a homogeneous current distribution even when the Fermi energy is tuned to the Dirac point, unlike ballistic graphene devices, where transport becomes dominated by edge modes [32,33]. Close scrutiny of

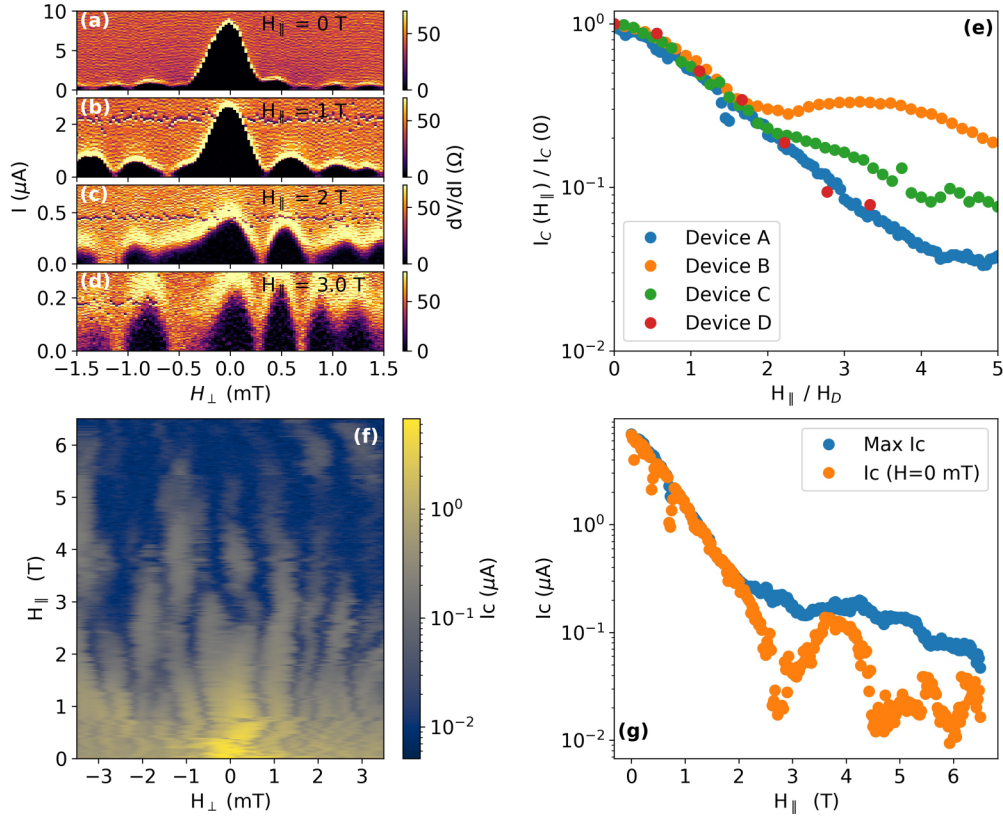


FIG. 3. (a)–(d) Differential resistance of junction A as a function of bias current and external perpendicular magnetic field, taken with applied in-plane magnetic field of 0, 1, 2, and 3 T, respectively. All measurements were conducted with  $V_G = 20$  V. (e) Parallel field dependence of the maximal critical current for junctions A, B, C, and D.  $I_c$  is normalized to  $I_c(H_{\parallel} = 0, H_{\perp} = 0)$ , and the in-plane field is normalized by a junction-specific decay field  $H_D$ . Each value is extracted from a 2D scan of  $R(V, H_{\perp})$  at a given  $H_{\parallel}$  and is defined as the maximal  $I_c$  obtained in each scan.  $H_D = 0.6, 0.16, 0.4,$  and  $0.9$  T for junctions A, B, C, and D, respectively. The field at which exponential decay slows  $H_T$  is indicated by a dotted line for junctions A, B, and C. (f)  $I_c$  of junction A as a function of  $H_{\parallel}$  and  $H_{\perp}$ . The curves were shifted to correct for sample misalignment and were then aligned to be as continuous as possible. Logarithmic color scale. (g) Dependence of the maximal  $I_c$  (blue) and of  $I_c$  at  $H_{\perp} = 0$  (orange), extracted from (f).

Figs. 2(d)–2(f), however, reveals discrepancies from the perfect interference pattern: lobes are not identical, and there is an asymmetry around  $H_{\perp} = 0$ . We suggest that this asymmetry in the interference pattern is due to spatial asymmetry in junction shape and disorder potential [11,34,35]. Additional asymmetry could arise due to the penetration of vortices into the junction area, breaking time reversal symmetry locally [36,37]. This will be more likely to contribute at finite  $H_{\parallel}$ . Having confirmed that 2DJJs have transport characteristics typical of diffusive SGS junctions [21], we turn our focus to the effect of in-plane magnetic field  $H_{\parallel}$  on the junction.

### III. TRANSPORT IN PARALLEL MAGNETIC FIELD

Since the junction is sensitive to out-of-plane fields  $H_{\perp}$  on the scale of a few hundreds of microteslas, extreme care is needed when aligning  $H_{\perp}$  and  $H_{\parallel}$  in our vector magnet to the sample geometric tilt. We do this by measuring the out-of-plane interference pattern at any given  $H_{\parallel}$ . At low fields of up to 1.5 T in junction A, the interference pattern shows a clearly distinguishable central lobe [Figs. 3(a) and 3(b)], allowing for unambiguous identification of the absolute field orientation. At higher  $H_{\parallel}$  this is no longer possible: the central lobe is suppressed to the same magnitude as the side lobes [Figs. 3(c)

and 3(d)]. This SQUID-like supercurrent distribution may be retained up to high parallel field. Junction A, for example, retains its critical current at a field of  $H_{\parallel} = 8.5$  T, showing a SQUID-like lobe structure as a function of  $H_{\perp}$  [Fig. 4(a)]. The voltage as a function of current curve shows a clear transition from the superconducting to normal state at a critical current of  $I = 100$  nA for  $H_{\perp} = -2$  mT [Fig. 4(b)].

Once the central lobe is no longer distinguishable, there is, in general, no straightforward indication of the true position of  $H_{\perp} = 0$ . Lacking this identification, we take the maximal  $I_c(H_{\perp})$  (hence  $I_c^{\max}$ ) as a measure for the junction critical current at each  $H_{\parallel}$ . We find that  $I_c^{\max}(H_{\parallel})$  exhibits an exponential-like decay, corresponding to the suppression of the central lobe seen in Figs. 3(a)–3(c). Normalizing to  $I_c^{\max}(H_{\parallel} = 0)$ , we plot  $I_c^{\max}(H_{\parallel})$  in Fig. 3(e) for junctions A, B, C, and D (all have monolayer graphene weak links, except junction B, which is bilayer graphene). To see the universality of the decay of  $I_c(H_{\parallel})$ , we normalize it by a junction-specific decay field  $H_D$ . The universal decay in  $I_c^{\max}$  persists up to a second characteristic field scale  $H_T$ , where  $I_c^{\max}$  stabilizes to the critical current of the side lobes. Depending on the sample, at  $H > H_T$  the exponential decay in  $I_c^{\max}$  either becomes moderate or even turns into a small increase. For junctions

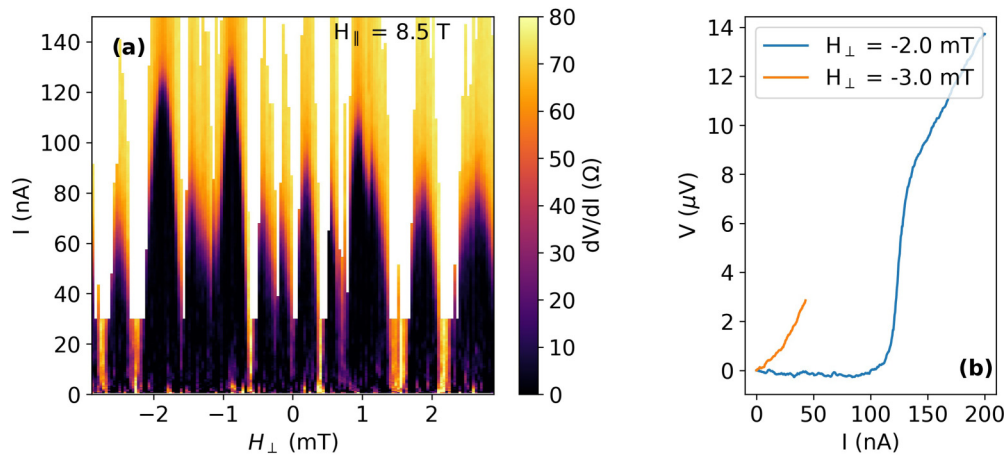


FIG. 4. High-field supercurrent. (a) The interference pattern of junction A at a parallel field of 8.5 T shows clear lobes of zero resistance (data are from a different cooldown than Fig. 3). (b)  $I$ - $V$  curve from (a) where the critical current is maximal (blue) and minimal (orange). The measurement was set to stop when the normal state transport was observed.

A, B, and C shown in Fig. 3(e) this field is given by  $H_T = 2.4$  T ( $4H_D$ ), 0.24 T ( $1.5H_D$ ), and 0.8 T ( $2H_D$ ), respectively. In junction D there are not enough data points to quantify this field. The junctions thus evolve to a SQUID-like lobe structure at finite, yet device-dependent  $H_{||}$  (see Supplemental Material, Sec. 3 [20]). The Zeeman effect in a uniform junction predicts universal decay with  $H_{||}$ . Deviation from universal behavior at  $H_T$  could be a result of ripples or junction nonuniformity, as we will discuss.

We now turn our attention to Fig. 3(f), which depicts the evolution of  $I_C$  vs  $H_{\perp}$  and  $H_{||}$  in junction A. In this junction we were able to track the evolution of the interference pattern up to  $H_{||} = 6.5$  T, aligning the  $I_C(H_{\perp})$  curves as explained in Sec. 1 of the Supplemental Material [20], thus obtaining the map shown in Fig. 3(f).<sup>1</sup> The magnitude of  $I_C(H_{||}, H_{\perp} = 0)$ , plotted in Fig. 3(g), shows a suppression and recovery pattern. These data are reminiscent of suppression-recovery patterns seen in superconductor-ferromagnet-superconductor (SFS) junctions [38–43] and in 2D systems [14,15,17], where they are interpreted as a  $0$ - $\pi$  transition.

The salient features of the data are therefore (1) exponential decay of the critical current at low field, (2) saturation of the critical current at intermediate fields, (3) lobe structure transition from Fraunhofer-like to SQUID-like, and (4) vanishing and reappearing of the central lobe critical current in device A. In what follows, we discuss the physics in our 2DJJ by considering both the parallel field-tunable Zeeman splitting of the graphene band structure and the orbital effect of out-of-plane ripples in the graphene [19].

#### IV. THEORETICAL MODEL AND DISCUSSION

Lacking an intrinsic spin-orbit coupling, graphene dispersion is affected by magnetic field only through Zeeman

splitting, where the Zeeman energy is analogous to the exchange interaction in SFS JJs [19,44]. In the latter, the superconducting order parameter in the ferromagnetic layer varies as the product of an exponential decay and an oscillatory term:

$$\psi(x) = \psi_i \exp(-k_1 x) \cos(k_2 x), \quad (2)$$

where  $\psi(x)$  is the order parameter at position  $x$  along the junction,  $\psi_i$  is the order parameter at the superconducting lead, and  $k_1$  and  $k_2$  are the inverse characteristic length scales associated with the decay and oscillation. In the diffusive limit, they are both given by  $1/k_1, 1/k_2 = \sqrt{L^2 E_{Th}/E_Z} = \sqrt{2D/g\mu_B H_{||}}$ , where  $D$  is the diffusion coefficient.

The order parameter thus experiences a decay accompanied by oscillation, with zeros occurring periodically when  $Lk_2 = \pi/2 + n\pi$  or  $E_Z = (\pi/2 + n\pi)^2 E_{Th}$ . This behavior of the order parameter leads to an oscillatory decay of the critical current of the junction. Following this intuition, the critical current of an SGS junction in a parallel magnetic field is thus expected to undergo an exponential suppression at low fields, in agreement with our observations. The oscillatory component of the wave function leads to a  $0$ - $\pi$  transition: a change in the equilibrium phase difference between the two superconducting leads, accompanied by a reversal of the supercurrent.

Using the analytical solution of the Usadel equations in an SGS junction [19] to qualitatively model our system, we calculate the critical current as a function of  $H_{||}$  and  $H_{\perp}$  specifically for junction A. We assume the junction length  $L = 214$  nm and width  $W = 4.69$   $\mu$ m [average dimensions are taken from the scanning electron microscopy (SEM) measurement shown in Fig. 1(c)]. Results are shown in Fig. 5(a). The assumed uniform supercurrent reversal manifests in the suppression of all lobes, corresponding to the disappearance of the uniform supercurrent throughout the junction at a numerically determined transition field [19]:

$$H_{||} \approx \frac{2.5E_{Th}}{0.5g\mu_B} = \frac{5D\hbar}{g\mu_B L^2}. \quad (3)$$

<sup>1</sup>Data in Figs. 3(a)–3(d) come from a different measurement than those in Fig. 3(f), taken on the same device, and show a slightly different lobe structure.

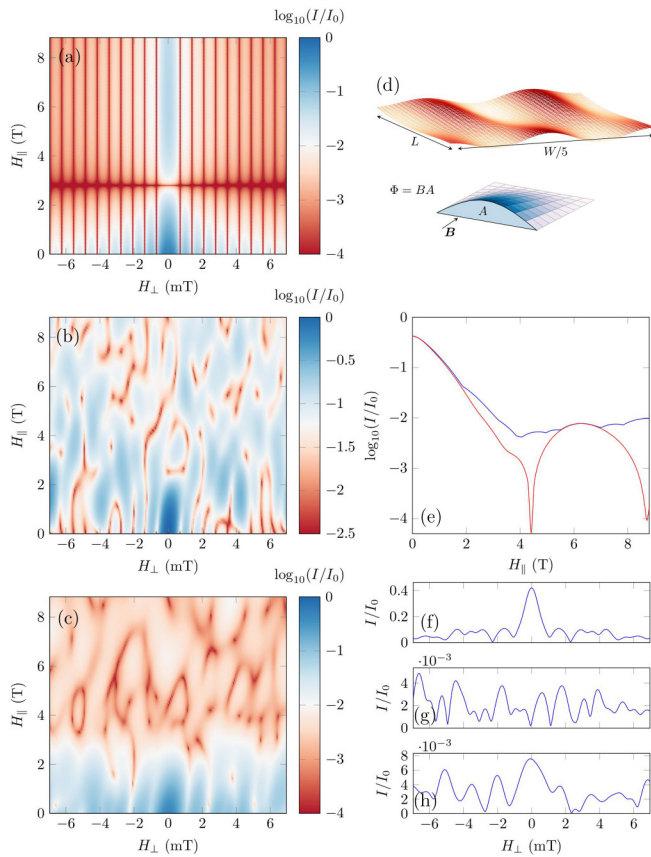


FIG. 5. (a)–(c) Calculated critical current  $I_c$  with a logarithmic color scale as a function of  $H_{\perp}$  and  $H_{\parallel}$ . (a) Simulated Zeeman effect with  $E_{Th} = 64 \mu\text{eV}$  and a rectangular junction of dimensions  $L = 214 \text{ nm}$ ,  $W = 4.69 \mu\text{m}$  without ripples. (b) A rectangular junction with ripples, disregarding the Zeeman effect. (c) Our measured junction contour with varying  $L$ ,  $E_{Th} = 64 \mu\text{eV}$ , Zeeman effect, and ripples. (d) Top: ripple profile used to generate the maps in (b) and (c). Note that the actual aspect ratio is around  $W/L = 20$ . Bottom: illustration of a long-wavelength ripple which could give rise to a zero in  $I_c$  at low fields. (e)  $I_c$  at  $H_{\perp} = 0$  (red) and maximal  $I_c$  for all  $H_{\perp}$  (blue) vs  $H_{\parallel}$ ; line cuts are taken from the simulation in (c). (f)–(h)  $I_c$  vs  $H_{\perp}$  for  $H_{\parallel} = 0, 4.1, \text{ and } 6.2 \text{ T}$ ; line cuts are from the simulation in (c).

From the experimentally observed transition field of 2.8 T, assuming  $g = 2$ , we find  $E_{Th} = 64 \mu\text{eV}$ . This falls between the order of magnitude expected for  $E_{Th}$  of hundreds of  $\mu\text{eV}$  which we extract from normal regime transport properties and  $E_{Th}^*$  of tens of  $\mu\text{eV}$  extracted from  $I_c R_N$ . Recalling that a lower effective  $E_{Th}$  has been attributed to Andreev reflection across an imperfect S-N interface, we point out that there is, to the best of our knowledge, no theory addressing how this would affect the Zeeman physics in the junction.

In the data in Fig. 3(f) we find that high-order lobes are retained, while the zero lobe, representing the average supercurrent, is suppressed. This indicates that the supercurrent is nonuniform. When multiple transport channels are present, they may carry positive and negative supercurrents which cancel out at  $H_{\parallel} = 2.8 \text{ T}$ , where the central lobe vanishes. In this regime the other lobes of the interference pattern, measuring higher moments of the supercurrent with respect

to the out-of-plane field, should not, in general, disappear. This phenomenon was seen in SFS JJs with a nonuniform ferromagnetic barrier, leading to a similar interference pattern [45–48]. Nonuniformity in supercurrent reversal can arise from local variation in  $E_{Th}$  since regions with lower  $E_{Th}$  will undergo stronger suppression due to  $E_Z$ . Such variation in  $E_{Th}$  can arise from varying junction length, as well as from local variations in contact transparency. Additionally, it could be a consequence of charge disorder, locally affecting the diffusion constant. However, the observed SQUID-like interference pattern can be reproduced only by an  $E_{Th}$  profile which sharply favors edge transport.

We now turn to the orbital effects associated with the locally varying perpendicular components of  $H_{\parallel}$ . These variations may be caused either by graphene height variations or by disruptions to the parallel field due to the Meissner effect, which diverts flux lines around the superconducting electrodes (flux focusing). Because both ripples and flux focusing give rise to a spatially varying perpendicular field component, their effects on the electric current are similar. For concreteness we give an in-depth discussion of the ripple scenario but note that the underlying mechanism could, in principle, also be flux focusing.

Using the same model as discussed previously, we distinguish between the effects of short- and long-wavelength ripples [19]. Short ripples as seen in microscopy studies of graphene on  $\text{SiO}_2$  are typically  $\approx 0.3 \text{ nm}$  peak to peak, with a correlation length of 10–30 nm [49–52]. Long ripples have a wavelength larger than the junction dimensions. Intuitively, one may gauge the effect of a ripple by calculating the flux accumulated within an area defined by the ripple lateral cross section, illustrated in Fig. 5(d). To induce a full current suppression and revival at  $H_{\perp} = 0$ , a ripple within the junction has to accumulate a single flux quantum due to the parallel field, according to the equation

$$H_{\parallel} = \frac{\Phi_0}{\eta\lambda}, \quad (4)$$

where  $\eta$  is the average ripple amplitude within the junction and  $\lambda$  is the wavelength (or the limiting junction dimension if the ripple extends beyond the junction). For the typical short-wavelength ripple seen in graphene on  $\text{SiO}_2$ , parallel fields of order 50 T are required to obtain an entire flux quantum within a ripple. However, the cumulative effect of many such ripples causes a faster decay of the critical current which can create exponential-like behavior, similar to the Zeeman effect [19].

Two-dimensional JJs in a parallel field are highly sensitive to long-wavelength height variations [19]. In our experimental geometry, with junction width  $W \approx 4.7 \mu\text{m}$ , it is possible to consider a ripple of length  $\lambda \simeq W$ . As a long-wavelength feature accumulates much more flux, it is possible to reach a flux quantum given a few-tesla parallel field and a small height variation of  $\eta \approx 0.1 \text{ nm}$  within the junction. We note that based on atomic force microscopy and scanning tunneling microscopy studies, it is difficult to tell whether such subnanometer height variations are present over micron length scales. Such geometry is physically conceivable due to strain or curvature of the substrate and cannot be ruled out. We show the simulated supercurrent in a sample ripple configuration containing ripples in Fig. 5(b). The simulation reproduces the

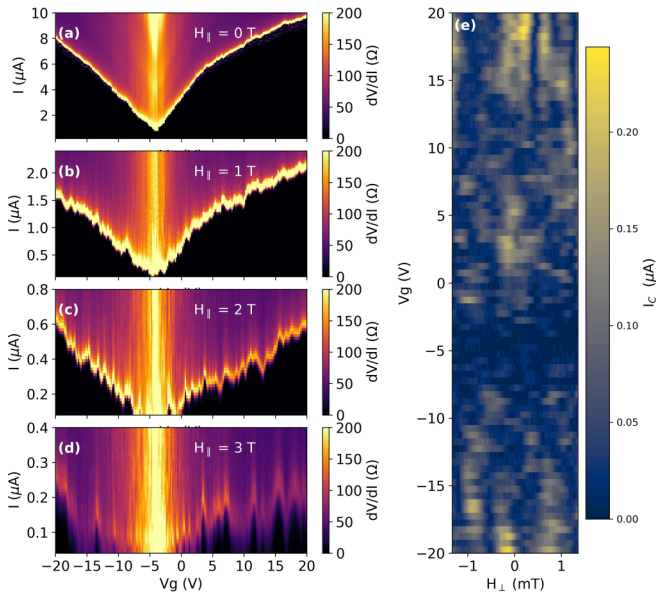


FIG. 6. (a)–(d) Differential resistance of junction A as a function of bias current and gate voltage, taken with applied in-plane magnetic field of 0, 1, 2, and 3 T, respectively. All measurements were conducted with  $H_{\perp} = 0$ . (e)  $I_C$  vs  $H_{\perp}$  and  $V_G$  for junction A, taken with parallel field  $H_{\parallel} = 3$  T.

features of the data highlighted previously: exponential decay followed by saturation, lobe structure transition, and a critical current dip at around  $B = 3$  T. The specifics of these features, such as the location and sharpness of the critical current dip, vary with different ripple configurations; however, many different patterns can produce qualitatively similar results (see Supplemental Material, Sec. 2 [20]). Figure 5(d) illustrates the specific ripple profile used to obtain the map in Fig. 5(b). The simulation does not include ripples of wavelength smaller than around 100 nm. These, in general, cause a sharper decay of critical current with parallel field [19].

Since we expect Zeeman and ripple effects to coexist, we present a compound simulation which considers them both [Fig. 5(c)]. This simulation also accounts for varying  $E_{Th}$  due to variation in the junction length as extracted from the SEM data presented in Fig. 1(c). In the case of varying junction length our analytical model is not rigorous, but it does give a qualitative approximation. As we see in Fig. 5(e), the simulation reproduces the exponential decay, suppression, and recovery of  $I_C(H_{\parallel}, H_{\perp} = 0)$ . The lobe structure at  $H_{\parallel} = 0, 4.1, 6.2$  T [Figs. 5(f)–5(h)] exhibits the experimentally observed transition between Fraunhofer-like and SQUID-like profiles.

## V. GATE DEPENDENCE IN MAGNETIC FIELD

Finally, we observe how the application of  $H_{\parallel}$  affects the gate dependence of the critical current (Fig. 6). At zero field  $I_C$  varies smoothly with  $V_G$  [Fig. 6(a)], leading to a nearly constant  $I_C R_N$  product away from the Dirac point. Upon increasing  $H_{\parallel}$ ,  $I_C$  fluctuates with  $V_G$  [Figs. 6(b)–6(d)] leading to

$H_{\parallel} = 3$  T to patterns of decay and revival of  $I_C(V_G)$ . Observing the evolution of the interference pattern with  $V_G$  at the same field reveals a qualitative change in the number of visible lobes and in their positions [Fig. 6(e)].

The observed gate dependence of the interference pattern shows that at  $H_{\parallel}$  around the suppression-recovery field of 2.8 T, the junction enters a new regime where the critical current survives in patches at fluctuating gate values. Similar phenomenology has been observed in ballistic graphene JJs at high perpendicular field and has been attributed to chaotic billiards due to cyclotron orbits reflecting from the graphene edge [53]. However, the physics in our regime is different since the junction is diffusive and  $B_{\perp} \approx 0$ . Within the Zeeman effect interpretation, it could be due to local gate-driven fluctuations around the  $0-\pi$  transition as in [16]. Alternatively, when ripples become important, changing gate could change the resulting interference pattern. There could also be a gate-dependent effect in the contact region between the graphene and NbSe<sub>2</sub>. In any case, clearly, the current flow distribution in this regime depends strongly on graphene Fermi energy. This could be linked to local charge conditions such as the disorder potential landscape; however, the lobe structure continues to evolve when the graphene is at high carrier densities, where disorder potential should be screened.

## VI. CONCLUSION

We conclude that the 2DJJ architecture allows the study of graphene Josephson junctions at high parallel magnetic fields, where supercurrent is sensitive to both the Zeeman effect and subnanometer graphene height variations. Junction currents evolve from a Fraunhofer-like to a SQUID-like interference pattern. We observe a supercurrent suppression and recovery feature which may be associated with a Zeeman-driven  $0-\pi$  transition or with the accumulation of a single flux quantum within a micron-wavelength ripple. While in the present measurements it is difficult to distinguish between the two effects, future experiments, with graphene placed on hexagonal boron nitride (hBN), are expected to suppress the ripple contribution. In the future it will be interesting to consider devices of the 2DJJ architecture utilizing different 2D materials as contacts and weak links. For example, devices where graphene inherits a spin-orbit term from a transition metal dichalcogenide substrate. The combination of significant spin-orbit and high parallel magnetic fields in the context of a Josephson junction could give rise to topological effects [54].

The authors wish to thank M. Aprili, Y. Oreg, A. Stern, F. Pientka, and A. Di Bernardo for illuminating discussions. This work was funded by a European Research Council Starting Grant (Grant No. 637298, TUNNEL), Israeli Science Foundation Grant No. 861/19, and BSF Grant No. 2016320. T.D. and A.Z. are grateful to the Azrieli Foundation for Azrieli Fellowships. K.W. and T.T. acknowledge support from the Elemental Strategy Initiative conducted by the MEXT, Japan, Grant No. JPMXP0112101001, JSPS KAKENHI Grant No. JP20H00354 and the CREST (Grant No. JPMJCR15F3), JST.

- [1] D. K. Efetov, L. Wang, C. Handschin, K. B. Efetov, J. Shuang, R. Cava, T. Taniguchi, K. Watanabe, J. Hone, C. R. Dean, and P. Kim, Specular interband Andreev reflections at van der Waals interfaces between graphene and NbSe<sub>2</sub>, *Nat. Phys.* **12**, 328 (2016).
- [2] M. R. Sahu, X. Liu, A. K. Paul, S. Das, P. Raychaudhuri, J. K. Jain, and A. Das, Inter-Landau-Level Andreev Reflection at the Dirac Point in a Graphene Quantum Hall State Coupled to a NbSe<sub>2</sub> Superconductor, *Phys. Rev. Lett.* **121**, 086809 (2018).
- [3] J. Lee, M. Kim, K. Watanabe, T. Taniguchi, G. H. Lee, and H. J. Lee, Planar graphene Josephson coupling via van der Waals superconducting contacts, *Curr. Appl. Phys.* **19**, 251 (2019).
- [4] X. Xi, Z. Wang, W. Zhao, J. H. Park, K. T. Law, H. Berger, L. Forró, J. Shan, and K. F. Mak, Ising pairing in superconducting NbSe<sub>2</sub> atomic layers, *Nat. Phys.* **12**, 139 (2016).
- [5] T. Dvir, F. Masee, L. Attias, M. Khodas, M. Aprili, C. H. L. Quay, and H. Steinberg, Spectroscopy of bulk and few-layer superconducting NbSe<sub>2</sub> with van der Waals tunnel junctions, *Nat. Commun.* **9**, 598 (2018).
- [6] T. Dvir, M. Aprili, C. H. L. Quay, and H. Steinberg, Zeeman Tunability of Andreev Bound States in van der Waals Tunnel Barriers, *Phys. Rev. Lett.* **123**, 217003 (2019).
- [7] J. Linder, T. Yokoyama, D. Huertas-Hernando, and A. Sudbø, Supercurrent Switch in Graphene  $\pi$  Junctions, *Phys. Rev. Lett.* **100**, 187004 (2008).
- [8] Q. Liang, Y. Yu, Q. Wang, and J. Dong, Controllable  $0-\pi$  Transition in a Superconducting Graphene-Nanoribbon Junction, *Phys. Rev. Lett.* **101**, 187002 (2008).
- [9] A. G. Moghaddam and M. Zareyan, Long-range Josephson coupling through ferromagnetic graphene, *Phys. Rev. B* **78**, 115413 (2008).
- [10] Y. Asano, T. Yoshida, Y. Tanaka, and A. A. Golubov, Electron transport in a ferromagnet-superconductor junction on graphene, *Phys. Rev. B* **78**, 014514 (2008).
- [11] H. J. Suominen, J. Danon, M. Kjaergaard, K. Flensberg, J. Shabani, C. J. Palmstrøm, F. Nichele, and C. M. Marcus, Anomalous Fraunhofer interference in epitaxial superconductor-semiconductor Josephson junctions, *Phys. Rev. B* **95**, 035307 (2017).
- [12] P. Fulde and R. A. Ferrell, Superconductivity in a strong spin-exchange field, *Phys. Rev.* **135**, A550 (1964).
- [13] A. I. Larkin and Y. N. Ovchinnikov, Inhomogeneous state of superconductors, *Zh. Eksp. Teor. Fiz.* **47**, 1136 (1964) [*Sov. Phys. JETP* **20**, 762 (1965)].
- [14] A. Q. Chen, M. J. Park, S. T. Gill, Y. Xiao, D. R. Plessis, G. J. MacDougall, M. J. Gilbert, and N. Mason, Finite momentum Cooper pairing in three-dimensional topological insulator Josephson junctions, *Nat. Commun.* **9**, 3478 (2018).
- [15] S. Hart, H. Ren, M. Kosowsky, G. Ben-Shach, P. Leubner, C. Brüne, H. Buhmann, L. W. Molenkamp, B. I. Halperin, and A. Yacoby, Controlled finite momentum pairing and spatially varying order parameter in proximitized HgTe quantum wells, *Nat. Phys.* **13**, 87 (2016).
- [16] C. T. Ke, C. M. Moehle, F. K. Vries, C. Thomas, S. Metti, C. R. Guinn, R. Kallagher, M. Lodari, G. Scappucci, T. Wang, R. E. Diaz, G. C. Gardner, M. J. Manfra, and S. Goswami, Ballistic superconductivity and tunable  $\pi$  junctions in InSb quantum wells, *Nat. Commun.* **10**, 3764 (2019).
- [17] C. Li, B. de Ronde, J. de Boer, J. Ridderbos, F. Zwanenburg, Y. Huang, A. Golubov, and A. Brinkman, Zeeman-Effect-Induced  $0-\pi$  Transitions in Ballistic Dirac Semimetal Josephson Junctions, *Phys. Rev. Lett.* **123**, 026802 (2019).
- [18] J. Linder, A. M. Black-Schaffer, and A. Sudbø, Triplet proximity effect and odd-frequency pairing in graphene, *Phys. Rev. B* **82**, 041409(R) (2010).
- [19] E. H. Fyhn, M. Amundsen, A. Zalic, T. Dvir, H. Steinberg, and J. Linder, Combined Zeeman and orbital effect on the Josephson effect in rippled graphene, *Phys. Rev. B* **102**, 024510 (2020).
- [20] See Supplemental Material at <http://link.aps.org/supplemental/10.1103/PhysRevB.103.115401> for the magnetic field alignment procedure (Sec. 1), information on the simulation of ripples in graphene (Sec. 2), measurements from additional samples (Sec. 3), and fabrication methods (Sec. 4).
- [21] H. B. Heersche, P. Jarillo-Herrero, J. B. Oostinga, L. M. K. Vandersypen, and A. F. Morpurgo, Bipolar supercurrent in graphene, *Nature (London)* **446**, 56 (2007).
- [22] D. Jeong, J. H. Choi, G. H. Lee, S. Jo, Y. J. Doh, and H. J. Lee, Observation of supercurrent in PbIn-graphene-PbIn Josephson junction, *Phys. Rev. B* **83**, 094503 (2011).
- [23] K. Komatsu, C. Li, S. Autier-Laurent, H. Bouchiat, and S. Guéron, Superconducting proximity effect in long superconductor/graphene/superconductor junctions: From specular Andreev reflection at zero field to the quantum Hall regime, *Phys. Rev. B* **86**, 115412 (2012).
- [24] C. T. Ke, I. V. Borzenets, A. W. Draelos, F. Amet, Y. Bomze, G. Jones, M. Craciun, S. Russo, M. Yamamoto, S. Tarucha, and G. Finkelstein, Critical current scaling in long diffusive graphene-based Josephson junctions, *Nano Lett.* **16**, 4788 (2016).
- [25] C. Li, S. Guéron, A. Chepelianskii, and H. Bouchiat, Full range of proximity effect probed with superconductor/graphene/superconductor junctions, *Phys. Rev. B* **94**, 115405 (2016).
- [26] J. C. Hammer, J. C. Cuevas, F. S. Bergeret, and W. Belzig, Density of states and supercurrent in diffusive SNS junctions: Roles of nonideal interfaces and spin-flip scattering, *Phys. Rev. B* **76**, 064514 (2007).
- [27] A. N. Tahvildar-Zadeh, J. K. Freericks, and B. K. Nikolić, Thouless energy as a unifying concept for Josephson junctions tuned through the Mott metal-insulator transition, *Phys. Rev. B* **73**, 184515 (2006).
- [28] E. Khestanova, J. Birkbeck, M. Zhu, Y. Cao, G. L. Yu, D. Ghazaryan, J. Yin, H. Berger, L. Forró, T. Taniguchi, K. Watanabe, R. V. Gorbachev, A. Mishchenko, A. K. Geim, and I. V. Grigorieva, Unusual suppression of the superconducting energy gap and critical temperature in atomically thin NbSe<sub>2</sub>, *Nano Lett.* **18**, 2623 (2018).
- [29] P. Dubos, H. Courtois, B. Pannetier, F. K. Wilhelm, A. D. Zaikin, and G. Schön, Josephson critical current in a long mesoscopic SNS junction, *Phys. Rev. B* **63**, 064502 (2001).
- [30] F. D. Callaghan, M. Laulajainen, C. V. Kaiser, and J. E. Sonier, Field Dependence of the Vortex Core Size in a Multiband Superconductor, *Phys. Rev. Lett.* **95**, 197001 (2005).
- [31] E. F. Talantsev, W. P. Crump, J. O. Island, Y. Xing, Y. Sun, J. Wang, and J. L. Tallon, On the origin of critical temperature enhancement in atomically thin superconductors, *2D Mater.* **4**, 025072 (2017).

- [32] M. T. Allen, O. Shtanko, I. C. Fulga, A. R. Akhmerov, K. Watanabe, T. Taniguchi, P. Jarillo-Herrero, L. S. Levitov, and A. Yacoby, Spatially resolved edge currents and guided-wave electronic states in graphene, *Nat. Phys.* **12**, 128 (2016).
- [33] M. J. Zhu, A. V. Kretinin, M. D. Thompson, D. A. Bandurin, S. Hu, G. L. Yu, J. Birkbeck, A. Mishchenko, I. J. Vera-Marun, K. Watanabe, T. Taniguchi, M. Polini, J. R. Prance, K. S. Novoselov, A. K. Geim, and M. Ben Shalom, Edge currents shunt the insulating bulk in gapped graphene, *Nat. Commun.* **8**, 6 (2017).
- [34] A. Rasmussen, J. Danon, H. Suominen, F. Nichele, M. Kjaergaard, and K. Flensberg, Effects of spin-orbit coupling and spatial symmetries on the Josephson current in SNS junctions, *Phys. Rev. B* **93**, 155406 (2016).
- [35] A. Assouline, C. Feuillet-Palma, N. Bergeal, T. Zhang, A. Mottaghizadeh, A. Zimmers, E. Lhuillier, M. Eddrie, P. Atkinson, M. Aprili, and H. Aubin, Spin-Orbit induced phase-shift in Bi<sub>2</sub>Se<sub>3</sub> Josephson junctions, *Nat. Commun.* **10**, 126 (2019).
- [36] T. Golod, A. Rydh, and V. M. Krasnov, Detection of the Phase Shift from a Single Abrikosov Vortex, *Phys. Rev. Lett.* **104**, 227003 (2010).
- [37] V. M. Krasnov, Josephson junctions in a local inhomogeneous magnetic field, *Phys. Rev. B* **101**, 144507 (2020).
- [38] T. Kontos, M. Aprili, J. Lesueur, F. Genêt, B. Stephanidis, and R. Boursier, Josephson Junction through a Thin Ferromagnetic Layer: Negative Coupling, *Phys. Rev. Lett.* **89**, 137007 (2002).
- [39] W. Guichard, M. Aprili, O. Bourgeois, T. Kontos, J. Lesueur, and P. Gandit, Phase Sensitive Experiments in Ferromagnetic-Based Josephson Junctions, *Phys. Rev. Lett.* **90**, 167001 (2003).
- [40] Y. Blum, A. Tsukernik, M. Karpovski, and A. Palevski, Oscillations of the Superconducting Critical Current in Nb-Cu-Ni-Cu-Nb Junctions, *Phys. Rev. Lett.* **89**, 187004 (2002).
- [41] V. A. Oboznov, V. V. Bol'ginov, A. K. Feofanov, V. V. Ryazanov, and A. I. Buzdin, Thickness Dependence of the Josephson Ground States of Superconductor-Ferromagnet-Superconductor Junctions, *Phys. Rev. Lett.* **96**, 197003 (2006).
- [42] V. Shelukhin, A. Tsukernik, M. Karpovski, Y. Blum, K. B. Efetov, A. F. Volkov, T. Champel, M. Eschrig, T. Löfwander, G. Schon, and A. Palevski, Observation of periodic  $\pi$ -phase shifts in ferromagnet-superconductor multilayers, *Phys. Rev. B* **73**, 174506 (2006).
- [43] J. W. A. Robinson, S. Piano, G. Burnell, C. Bell, and M. G. Blamire, Critical Current Oscillations in Strong Ferromagnetic  $\pi$  Junctions, *Phys. Rev. Lett.* **97**, 177003 (2006).
- [44] A. I. Buzdin, Proximity effects in superconductor-ferromagnet heterostructures, *Rev. Mod. Phys.* **77**, 935 (2005).
- [45] M. Kemmler, M. Weides, M. Weiler, M. Opel, S. T. B. Goennenwein, A. S. Vasenko, A. A. Golubov, H. Kohlstedt, D. Koelle, R. Kleiner, and E. Goldobin, Magnetic interference patterns in  $0-\pi$  superconductor/insulator/ferromagnet/superconductor Josephson junctions: Effects of asymmetry between  $0$  and  $\pi$  regions, *Phys. Rev. B* **81**, 054522 (2010).
- [46] S. M. Frolov, D. J. Van Harlingen, V. V. Bolginov, V. A. Oboznov, and V. V. Ryazanov, Josephson interferometry and Shapiro step measurements of superconductor-ferromagnet-superconductor  $0-\pi$  junctions, *Phys. Rev. B* **74**, 020503(R) (2006).
- [47] J. Pfeiffer, M. Kemmler, D. Koelle, R. Kleiner, E. Goldobin, M. Weides, A. K. Feofanov, J. Lisenfeld, and A. V. Ustinov, Static and dynamic properties of  $0$ ,  $\pi$ , and  $0-\pi$  ferromagnetic Josephson tunnel junctions, *Phys. Rev. B* **77**, 214506 (2008).
- [48] M. Weides, M. Kemmler, H. Kohlstedt, R. Waser, D. Koelle, R. Kleiner, and E. Goldobin,  $0-\pi$  Josephson Tunnel Junctions with Ferromagnetic Barrier, *Phys. Rev. Lett.* **97**, 247001 (2006).
- [49] M. Ishigami, J. H. Chen, W. G. Cullen, M. S. Fuhrer, and E. D. Williams, Atomic structure of graphene on SiO<sub>2</sub>, *Nano Lett.* **7**, 1643 (2007).
- [50] V. Geringer, M. Liebmann, T. Echtermeyer, S. Runte, M. Schmidt, R. Rückamp, M. C. Lemme, and M. Morgenstern, Intrinsic and Extrinsic Corrugation of Monolayer Graphene Deposited on SiO<sub>2</sub>, *Phys. Rev. Lett.* **102**, 076102 (2009).
- [51] W. G. Cullen, M. Yamamoto, K. M. Burson, J. H. Chen, C. Jang, L. Li, M. S. Fuhrer, and E. D. Williams, High-Fidelity Conformation of Graphene to SiO<sub>2</sub> Topographic Features, *Phys. Rev. Lett.* **105**, 215504 (2010).
- [52] J. Xue, J. Sanchez-Yamagishi, D. Bulmash, P. Jacquod, A. Deshpande, K. Watanabe, T. Taniguchi, P. Jarillo-Herrero, and B. J. LeRoy, Scanning tunneling microscopy and spectroscopy of ultra-flat graphene on hexagonal boron nitride, *Nat. Mater.* **10**, 282 (2011).
- [53] M. B. Shalom, M. J. Zhu, V. I. Fal, A. Mishchenko, A. V. Kretinin, K. S. Novoselov, C. R. Woods, K. Watanabe, T. Taniguchi, A. K. Geim, and J. R. Prance, Quantum oscillations of the critical current and high-field superconducting proximity in ballistic graphene, *Nat. Phys.* **12**, 318 (2016).
- [54] T. Wakamura, N. J. Wu, A. D. Chepelianskii, S. Guéron, M. Och, M. Ferrier, T. Taniguchi, K. Watanabe, C. Mattevi, and H. Bouchiat, Spin-Orbit-Enhanced Robustness of Supercurrent in Graphene/WS<sub>2</sub> Josephson Junctions, *Phys. Rev. Lett.* **125**, 266801 (2020).